

# HIGH ENERGY GAMMA-RAY OBSERVATIONS OF THE CRAB NEBULA AND PULSAR WITH THE SOLAR TOWER ATMOSPHERIC CHERENKOV EFFECT EXPERIMENT

S. Oser<sup>1,2</sup>, D. Bhattacharya<sup>3</sup>, L. M. Boone<sup>4</sup>, M. C. Chantell<sup>1</sup>, Z. Conner<sup>1,5</sup>, C. E. Covault<sup>1</sup>, M. Dragovan<sup>1,6</sup>, P. Fortin<sup>8</sup>, D. T. Gregorich<sup>7</sup>, D. S. Hanna<sup>8</sup>, R. Mukherjee<sup>9</sup>, R. A. Ong<sup>1</sup>, K. Ragan<sup>8</sup>, R. A. Scalzo<sup>1</sup>, D. R. Schuette<sup>1</sup>, C. G. Théoret<sup>8</sup>, T. O. Tümer<sup>3</sup>, D. A. Williams<sup>4</sup>, and J. A. Zweerink<sup>3</sup>

## ABSTRACT

The Solar Tower Atmospheric Cherenkov Effect Experiment (STACEE) is a new ground-based atmospheric Cherenkov telescope for gamma-ray astronomy. STACEE uses the large mirror area of a solar heliostat facility to achieve a low energy threshold. A prototype experiment which uses 32 heliostat mirrors with a total mirror area of  $\sim 1200 \text{ m}^2$  has been constructed. This prototype, called STACEE-32, was used to search for high energy gamma-ray emission from the Crab Nebula and Pulsar. Observations taken between November 1998 and February 1999 yield a strong statistical excess of gamma-like events from the Crab, with a significance of  $+6.75\sigma$  in 43 hours of on-source observing time. No evidence for pulsed emission from the Crab Pulsar was found, and the upper limit on the pulsed fraction of the observed excess was  $< 5.5\%$  at the 90% confidence level. A subset of the data was used to determine the integral flux of gamma rays from the Crab. We report an energy threshold of  $E_{th} = 190 \pm 60 \text{ GeV}$ , and a measured integral flux of  $I(E > E_{th}) = (2.2 \pm 0.6 \pm 0.2) \times 10^{-10} \text{ photons cm}^{-2} \text{ s}^{-1}$ . The observed flux is in agreement with a continuation to lower energies of the power law spectrum seen at TeV energies.

---

<sup>1</sup>Enrico Fermi Institute, University of Chicago, Chicago, IL 60637, USA.

<sup>2</sup>present address: Department of Physics and Astronomy, University of Pennsylvania, Philadelphia, PA 19104, USA.

<sup>3</sup>Institute of Geophysics and Planetary Physics, University of California, Riverside, CA 92521, USA.

<sup>4</sup>Santa Cruz Institute for Particle Physics, University of California, Santa Cruz, CA 95064, USA.

<sup>5</sup>present address: Department of Physics/Women and Power Leadership Programs, The George Washington University, Washington DC 20007, USA.

<sup>6</sup>present address: Jet Propulsion Lab, Pasadena, CA 91109, USA.

<sup>7</sup>Department of Physics and Astronomy, California State University, LA, Los Angeles, CA 90032, USA.

<sup>8</sup>Department of Physics, McGill University, Montreal, QC H3A 2T8, Canada.

<sup>9</sup>Department of Physics & Astronomy, Barnard College & Columbia University, New York, NY 10027, USA.

*Subject headings:* gamma rays: observations—ISM: individual (Crab Nebula)—pulsars: individual (Crab Pulsar)

## 1. INTRODUCTION

The Crab Nebula is the most studied object in the gamma-ray sky. Numerous ground-based experiments have detected emission from the Crab at energies from 300 GeV through 50 TeV. In addition, the EGRET detector on the Compton Gamma Ray Observatory has measured the spectrum of unpulsed gamma rays from the Crab up to an energy of  $\sim 10$  GeV (Nolan et al. 1993). High energy gamma rays are believed to result from inverse Compton scattering of relativistic electrons on synchrotron photons, thermal dust photons, and cosmic microwave photons. Such inverse Compton models have been described by de Jager & Harding (1992), Atoyan & Aharonian (1996), and de Jager et al. (1996). Under this scenario, high energy electrons are accelerated at the pulsar wind termination shock. They then propagate through the nebula, producing both synchrotron and inverse Compton emission.

In addition to unpulsed gamma rays, EGRET has also seen pulsed gamma-ray emission from the Crab (Nolan et al. 1993; Ramanamurthy et al. 1995; Fierro et al. 1998), which is assumed to be produced by the pulsar. Pulsed emission has not been seen at higher energies accessible to ground-based experiments (Lessard et al. 1999). The measurements require that pulsed emission cut off somewhere between 10 GeV and  $\sim 250$  GeV. Polar Cap models of pulsar emission (Daugherty & Harding 1982) predict sharp cutoffs near 10 GeV, whereas Outer Gap models (Cheng, Ho, & Ruderman 1986; Romani 1996) predict pulsed emission as high as  $\sim 50$  GeV.

No previous gamma-ray detector has had sensitivity to gamma rays at energies between  $\sim 10$  GeV and  $\sim 300$  GeV. Nonetheless, there are strong motivations to observe the Crab in this energy range, not only to test inverse Compton models at previously unexplored energies, but also to search for pulsed gamma-ray emission that could distinguish between pulsar emission models. Satellite experiments have been limited to energies below  $\sim 10$  GeV by low statistics because of their small apertures and the rapidly falling flux of gamma rays. Ground-based experiments, which detect gamma rays by the Cherenkov light produced in extensive air showers initiated by the gamma ray, typically have energy thresholds of  $\sim 300$  GeV. The energy threshold is limited by the ability of the instrument to distinguish dim flashes of Cherenkov light amidst the fluctuations in night sky background light. From signal-to-noise considerations, the energy threshold of an atmospheric Cherenkov telescope can be shown to behave like

$$E_{th} \propto \sqrt{\frac{\Phi \Omega \tau}{\epsilon A}}. \quad (1)$$

Here,  $\Phi$  is the flux of night sky background light,  $\Omega$  is the field of view of the instrument,  $\tau$  is the length of the electronic trigger coincidence window,  $\epsilon$  is the efficiency for detecting Cherenkov

photons, and  $A$  is the total mirror collection area of the instrument (Weekes 1988). In particular, the number of Cherenkov photons collected from a shower will scale with the mirror area  $A$ , while fluctuations in the night sky background light will increase with the square root of the light collection, and hence with  $\sqrt{A}$ . Thus, the energy threshold of an atmospheric Cherenkov detector decreases approximately in proportion to the inverse square root of the total mirror area.

The Solar Tower Atmospheric Cherenkov Effect Experiment (STACEE) is a new atmospheric Cherenkov detector for gamma-ray astronomy which uses the large mirror area of a solar power research facility to achieve a low energy threshold. STACEE uses an array of steerable mirrors, called heliostats, to collect Cherenkov light produced in extensive air showers. Heliostats focus the light onto secondary mirrors on a central tower, which image the light onto photomultiplier tube cameras (see Figure 1). Previous tests demonstrate that heliostat arrays can be used to detect Cherenkov light from extensive air showers (Ong et al. 1996; Chantell et al. 1998). Here we report on observations of the Crab Nebula and Pulsar taken with a prototype version of the STACEE instrument. This prototype, called STACEE-32, used 32 heliostats and a preliminary electronic trigger system. The full instrument incorporates 64 heliostats, and is presently under construction. It will start regular observations in the fall of 2000.

## 2. DETECTOR

STACEE is located at the National Solar Thermal Test Facility (NSTTF), at Sandia National Laboratories in Albuquerque, NM, USA (34.962° N, 106.509° W, 1705 m above sea level). The NSTTF is a solar power research facility of the U.S. Department of Energy. It includes 212 heliostat mirrors, each  $\sim 37\text{ m}^2$  in area, arrayed across a  $300\text{ m} \times 120\text{ m}$  area (see Figure 2). For solar power research, heliostats track the Sun and concentrate sunlight onto a central receiver tower. At night, STACEE-32 used a subset of the heliostats to track a gamma-ray source. These heliostats reflected Cherenkov light towards two 1.9 m diameter secondary mirrors near the top of the tower. The secondary mirrors concentrated light from the heliostats onto phototube cameras. Each photomultiplier tube (PMT) received light from a single heliostat in the array. The heliostats were tilted inwards to track “shower maximum,” the point of maximum air shower development (about 11 km above sea level for vertical showers). Details of the site, heliostats, secondary mirrors, and cameras are given elsewhere (Chantell et al. 1998; Oser 2000).

Each camera contained 16 photomultiplier tubes and received light from a separate portion of the heliostat field (see Figure 2). Solid acrylic light collectors based on the Dielectric Total Internal Reflecting Concentrator design (Ning, Winston, & O’Gallagher 1987) were placed in front of the PMTs. The collectors concentrated incident light onto 5 cm diameter photomultiplier tubes and restricted the field of view of each PMT on the secondary mirror. The field of view of a heliostat was determined by the diameter viewed by its PMT on the secondary mirror, divided by the distance between the secondary mirror and the heliostat. The fields of view were adjusted so that each heliostat saw a solid angle of approximately  $1.2 \times 10^{-4}$  sr on the sky.

The photomultiplier tubes (Photonis XP2282B model) had bi-alkali photocathodes with peak sensitivity near 400 nm and excellent time response ( $\sim 1$  ns resolution). The single photoelectron rate from night sky noise on each tube was  $\sim 1.5$  GHz, and the typical operating gain was  $1.1 \times 10^5$ . Signals from the PMTs were AC-coupled and amplified ( $\times 100$ ) and then routed to electronics racks inside the tower.

In order to achieve a low energy threshold, the PMT signals must be combined in a short time coincidence (see eq. [1]). The heliostats are at varying distances from the tower, and light from an air shower strikes different heliostats at different times, depending on the orientation of the shower. Therefore, signals from different heliostats must be delayed by varying amounts in order to put them into time coincidence. STACEE-32 used a two-level digital trigger to form this coincidence. The 32 heliostats were divided into four compact subclusters of eight heliostats each, as indicated in Figure 2. PMT signals were discriminated, and the discriminator outputs were individually delayed to put the eight signals within a subcluster into time coincidence with one another. If five of eight tubes fired within a 12.5 ns window, then that subcluster triggered. The four subcluster triggers were themselves delayed and put into time coincidence. Three of four subclusters firing within a 15 ns window resulted in an experiment trigger, which initiated readout. Thus, a total of at least fifteen heliostats had to fire to trigger the detector. The discriminator threshold was chosen so that the accidental trigger rate due to night sky background fluctuations was negligible ( $< 0.002$  Hz). The typical discriminator level was  $\sim 170$  mV, which was approximately 5.5 times the mean single photoelectron amplitude. The mean discriminator counting rate in each channel was  $\sim 2$  MHz.

Multi-hit time-to-digital converters (Lecroy 3377 TDC) measured the arrival times of pulses from each discriminator channel. Charge-integrating analog-to-digital converters (Lecroy 2249SG ADC) on 24 channels measured the pulse charge over a 37 ns integration gate. The long delay times in the trigger formation ( $\sim 1 \mu$ s) required that the ADC inputs be first routed through  $\sim 1200$  ns of high quality RG213 coaxial cable. These cables delayed the arrival of the pulses at the ADC until after the trigger had formed. Scaler counters recorded the PMT and subcluster trigger rates, and a GPS clock recorded the Universal Time for each event trigger. The PMT currents were also read out for every event. An experiment trigger asserted a veto, which inhibited further triggers until the event was read out and the veto was cleared by the data acquisition (DAQ) system. Counters measured the livetime of the experiment (the fraction of time for which triggers were enabled). The experiment was also triggered with an external pulser every two seconds to collect a sample of non-Cherenkov events for calibration purposes. All readout and control was done via an interface to a Silicon Graphics workstation. Details of the electronics are given in Oser (2000).

Calibration systems for STACEE-32 included a nitrogen laser and an LED flasher circuit. Optical fibers carried pulses from the laser to small wavelength shifter plates mounted at the center of each secondary mirror. The laser light pulsed all phototubes in each camera simultaneously. A filter wheel was used to attenuate the laser light level, and the slewing responses of the PMTs (time versus pulse amplitude) were so determined. On an occasional basis, the LED flasher was placed in front of each PMT to measure its gain *in situ*. Phototubes, delay modules, and other electronics

systems were also calibrated extensively in the lab before installation. In addition, the orientations and status of all heliostats were logged during tracking, and any malfunctions were noted offline and the affected data were identified.

### 3. EVENT RECONSTRUCTION AND BACKGROUND REJECTION

Although the energy threshold of an atmospheric Cherenkov detector is ultimately limited by night sky background light, the sensitivity of the detector is limited by a different kind of background, namely, cosmic ray air showers. STACEE-32’s high-multiplicity trigger coincidence effectively eliminated all accidental triggers due to fluctuations in night sky light. The high multiplicity of the trigger also rejected approximately 98% of all Cherenkov showers initiated by cosmic rays (see § 3.2). The remaining cosmic ray triggers form the background from which gamma-ray events must be distinguished.

Traditional atmospheric Cherenkov telescopes use a single mirror with a pixellated phototube camera. Each element in the camera is mapped to a different angular region on the sky, and thus one records an image of the Cherenkov shower in the sky. However, STACEE is not an imaging detector. Instead, the experiment is a lateral array which samples the Cherenkov wavefront at many locations within the light pool. In this respect, event reconstruction must be handled quite differently than for an imaging Cherenkov telescope. STACEE records the arrival time and photon density of the Cherenkov wavefront at each heliostat for every event. From these quantities the shape and lateral density profile of the Cherenkov light pool are determined. For STACEE-32, the charge resolution on the ADC measurements was limited by the high night sky light levels and relatively long integration gates. The charge resolution had a typical value of 8 photoelectrons. This resolution was not adequate for reconstructing the lateral density profile for most events, and so the ADCs were used only for slewing corrections and diagnostics. The full STACEE detector will use 1 GHz waveform digitizers, which will provide greatly improved resolution and allow reconstruction of the lateral density profile. For STACEE-32, event reconstruction was based solely upon timing information.

#### 3.1. Timing Reconstruction

Multi-hit TDCs measured the arrival times of PMT pulses. For each channel, the signal propagation times through the electronics were calibrated, and thus the expected arrival time of each Cherenkov pulse could be calculated, relative to the trigger time. We defined a time window with 12 ns width centered around the expected hit location. A heliostat which had a TDC hit within its time window is said to have an “in-time hit.” Some channels did not have in-time hits, if those heliostats were not hit by the air shower, or if the Cherenkov pulse failed to exceed the discriminator threshold. For every in-time hit, we reconstructed the arrival time of the Cherenkov

pulse at the heliostat by correcting for the transit time of light between the heliostat and the PMT, and the calibrated transit time of the PMT pulse through the electronics. ADC measurements were used to apply a slewing correction to those channels which had ADCs. The values of the slewing correction were determined from laser calibrations.

From the shape and orientation of the reconstructed timing wavefront at the heliostats, we determined the incident direction of the primary which initiated the air shower. At high energies ( $E > 1$  TeV), the Cherenkov-emitting core of the air shower extends through the atmosphere like a line source, and the resulting Cherenkov wavefront has a conical shape. At lower energies, however, the shower does not penetrate very far into the atmosphere, and most of the Cherenkov light is produced near the location of shower maximum. For this situation, the air shower approximates a point source of Cherenkov light, and the resulting wavefront has a more spherical shape. A ray drawn between the center of the light pool on the ground and the center of this sphere will point back towards the gamma-ray source.

The timing wavefront of each triggering event was fit to a spherical shape. Only those heliostats which had an in-time hit and a slewing-corrected time were used in the fit. The timing resolution for each channel was estimated from its discriminator rate on an event-by-event basis. Calibration runs taken with cosmic ray triggers showed that the timing resolution for channel  $i$  was related to its rate  $R_i$  by an empirical relation:

$$\sigma_{t,i} = \sigma_{0,i} \sqrt{1 + \left( \frac{R_i}{R_{0,i}} \right)^2} . \quad (2)$$

The constants  $\sigma_{0,i}$  and  $R_{0,i}$  were determined for each channel from the calibration data. Using the estimated timing resolution, the corrected times were fit to a sphere by a least squares fitting procedure. The location of the sphere's center was allowed to vary, but the radius of the sphere was constrained to a distance corresponding to a slant depth of  $271 \text{ g cm}^{-2}$  from the top of the atmosphere. This radius corresponds to the average location of shower maximum for a 100 GeV gamma ray. The fit was done three times in an iterative manner, first excluding points lying 4 standard deviations from the original fit, and then excluding any remaining points lying more than 4.5 standard deviations from the second fit.

For STACEE-32, the angular resolution was dominated by uncertainties in the determination of the center, or core, of the Cherenkov light pool. For gamma-ray air showers, the lateral density profile is quite smooth, and it is difficult to determine its center. For this analysis, we assumed the core location for all events to be at the geometric center of the array. Monte Carlo simulations indicate that STACEE-32 had an angular resolution of  $\sim 0.25^\circ$  for 200 GeV gamma rays. The field of view of the instrument was only  $0.35^\circ$  (half-angle), and therefore selecting events based on the reconstructed direction would not result in any significant improvement in the significance of a detection. However, the mean direction of air showers reconstructed by STACEE-32 was within  $0.1^\circ$  of the expected pointing direction, which verified the absolute pointing of the instrument to that accuracy.

### 3.2. Hadronic Rejection

Traditional imaging atmospheric Cherenkov telescopes for gamma-ray astronomy reject cosmic ray background events based on the orientation and width of the shower image in the camera. As a non-imaging Cherenkov telescope, STACEE uses very different means for statistically identifying and removing cosmic ray events.

Cosmic ray showers differ from gamma-ray showers in the total amount of Cherenkov light they produce. A gamma-ray shower produces, on average, significantly more Cherenkov photons than a cosmic ray of the same energy (see Figure 3). This effect happens because the nuclear cascade of a cosmic ray air shower contains fewer Cherenkov-producing particles than the electromagnetic cascade of a gamma-ray air shower, and because the energy threshold for Cherenkov light production is higher for nucleons than for electrons. Furthermore, the difference in the Cherenkov yield between gamma-ray showers and cosmic ray showers increases as the primary energy decreases. Gamma-ray air showers are brighter and trigger the detector with much greater efficiency than cosmic ray showers.

In addition, there are large differences between the lateral density profiles of the Cherenkov light in gamma-ray and cosmic ray events. Air shower simulations show that gamma-ray showers produce smooth and uniform light pools on the ground. In contrast, cosmic ray showers produce non-uniform light distributions. In these showers, a large proportion of the light is often concentrated in a small area on the ground. STACEE-32’s trigger required 15 heliostats to be hit simultaneously across the array, and it therefore imposed a uniformity requirement. The high multiplicity requirement of the trigger thus selected the smooth, gamma-like events, and rejected most of the irregular, hadron-like events. Measured cosmic ray rates and Monte Carlo simulations suggest a trigger rejection factor of  $\sim 50$  for cosmic rays, compared to gamma rays with the same energy spectrum. Nonetheless, there were additional hadronic cuts that were applied offline to further suppress the hadronic background.

Two hadronic cuts were developed for STACEE-32. The first cut was a trigger re-imposition cut. After in-time hits were found for each event (as described in § 3.1), the trigger multiplicity requirement was re-imposed. The in-time hit window (12 ns wide) was smaller than the trigger coincidence width, and thus re-imposing the trigger in software removed some events that passed the hardware trigger. Hadronic air showers have wider, more irregular timing profiles than gamma-ray showers, and so re-imposing the trigger with a narrower time window modestly increases the signal-to-noise for gamma rays. This cut also reduces the impact of any random PMT hits that occur in coincidence with actual air showers.

The second event cut used the shape of the timing wavefront to distinguish between gamma-ray showers and cosmic ray showers. As described above, gamma-ray showers have smooth, approximately spherical, timing profiles. Cosmic ray showers tend to have more irregular, less spherical wavefronts (see Figure 4). The goodness-of-fit of a spherical shape to the wavefront was used to distinguish between gamma rays and cosmic rays. We selected events based on the value of the chi-squared per degree of freedom ( $\chi^2/\text{ndf}$ ) of the spherical fit used for angular reconstruction.

This selection should further increase the signal-to-noise of a gamma-ray signal.

## 4. OBSERVATIONS

The STACEE-32 instrument observed the Crab extensively between 1998 November 15 and 1999 February 18. Data were taken on clear and moonless nights. We required the Crab to be within  $45^\circ$  of zenith. We took calibration data during times when Crab was low in the sky. Weather conditions and the presence of clouds were monitored regularly.

STACEE uses an ON-OFF observing strategy. Off-source runs are used to estimate the cosmic ray background level. A signal for gamma-rays shows up as an excess of ON events, compared to OFF events. On-source runs of 28 minutes length were taken with the heliostats tracking the gamma-ray source. Off-source runs were taken with the instrument tracking a point in the sky displaced by one half hour in right ascension from the gamma-ray source, but at the same declination. For each on-source run we took an off-source run of the same length. Together these two runs form an ON-OFF pair. The ON half of the pair preceded or followed the OFF half by exactly one half hour, and so both halves of the pair tracked the same trajectory in local coordinates on the sky. During these observations, STACEE-32 acquired a total of 141 ON-OFF pairs, corresponding to  $\sim 65$  hours of on-source observing time.

### 4.1. Run Cuts

In order to do a valid background subtraction, the ON and OFF halves of each pair must be closely matched in terms of detector properties and weather conditions. A series of run cuts were imposed to remove pairs affected by changing conditions.

Run cuts were designed to remove data with poor or changing weather, detector malfunctions, or high or fluctuating PMT rates. Run pairs affected by weather conditions were identified from observing logs. Given the relative proximity of the city of Albuquerque, clouds reflect artificial lighting, and change the apparent sky brightness. Observing logs identified six ON-OFF pairs taken under partially cloudy conditions. These were removed from the data set. Another pair was removed because atmospheric haze was noted. Yet another pair coincided with the arrival of a major high-pressure front, which changed the atmospheric conditions on a short timescale. Finally, on a single night, frost developed on the heliostats, and four run pairs from that night were discarded. In all, twelve ON-OFF pairs were removed because of weather conditions.

Major detector malfunctions affected a small number of runs. Two pairs had corrupted data because of failures in the DAQ system. Runs in which multiple heliostats malfunctioned in a single subcluster were also discarded. In these runs, the affected subcluster had a relatively low efficiency for participating in the trigger because its effective coincidence level was tightened from 5 of 8



tubes to 5 of 6 tubes. Five pairs were removed on this basis. Runs in which a single heliostat malfunctioned, or in which two heliostats in different subclusters malfunctioned, were left in the data set, although the affected heliostats were removed from event reconstruction for both halves of the ON-OFF pair, as described in § 4.2 below. Heliostat malfunctions were almost always repaired the following day.

High PMT rates degrade data in several ways. As equation [2] shows, the timing resolution worsens with increasing rate. The rate of accidental coincidences, completely negligible under normal operating conditions, increases rapidly with rising PMT rates. Finally, high rates increase deadtime in the subcluster trigger delay electronics. Runs with high rates were identified from their subcluster trigger rates. Typical runs have subcluster rates of  $\sim 1$  kHz. All runs in which the mean trigger rate for any subcluster exceeded 20 kHz were removed. If the RMS variation of a subcluster’s rate within the run exceeded 3 kHz, the run was also removed. These stringent cuts ensure that the accidental trigger rate remained  $< 0.01$  Hz, and that the deadtime in the trigger delay of each subcluster was  $< 1\%$ . Twenty ON-OFF pairs were removed by these cuts.

Finally, the data were scanned for runs with abnormally low event trigger rates. A single anomalous run was identified with a trigger rate about eight standard deviations below that of similar runs. The low rate is indicative of a detector malfunction, the cause of which is under investigation. The pair containing this anomalous run was removed from the final data set.

Run cuts were applied in a blind fashion, before the significance of any possible gamma-ray excess was determined, so as not to bias the result. After application of run cuts, 101 ON-OFF pairs remain in the data set. Table 1 summarizes the various run cuts.

## 4.2. PMT Cuts

It was not uncommon for a single heliostat or electronics channel to malfunction. Removing the entire run in this circumstance is rather draconian, and unnecessarily reduces the data set. Instead, bad channels were identified on a run-by-run basis. Offending channels were then removed from the offline analysis in both the ON and OFF halves of the run pair, and the data were analyzed as if the PMT were simply turned off. The most common problems were heliostat tracking errors, which could be identified from the heliostat log files. Removing the bad channels from both halves of a pair ensures that the ON and OFF pairs are balanced in terms of detector response.

## 5. RESULTS

After run cuts, the final STACEE-32 data set consists of 101 ON-OFF pairs, with a total on-source observing time of 155,335 s ( $\sim 43$  hours). Each run was processed separately, and event reconstruction proceeded as described in § 3. For each event, the GPS event time, fitted shower

direction, and  $\chi^2/\text{ndf}$  of the spherical fit were found. The livetime fraction for each run was calculated, and the event totals for each run were corrected for deadtime by dividing by the livetime fraction (typically between 88% and 92%).

A gamma-ray signal shows up as an excess of events in the ON runs, compared to the OFF runs. As described in § 3.2, two kinds of event cuts were used to enhance any potential gamma-ray signal. The first cut was to re-impose the trigger multiplicity in software. The second cut was based on the  $\chi^2/\text{ndf}$  of a spherical fit to the wavefront’s shape. Monte Carlo simulations suggest that a cut of  $\chi^2/\text{ndf} < 1$  will maximize the signal-to-noise.

### 5.1. Unpulsed Emission

First we performed a search for unpulsed emission, presumed to originate in the nebula of the Crab. The number of events in the on-source and off-source runs were tallied, with and without event cuts. Table 2 summarizes the results. The raw data show a strong excess of 4860 events, before event cuts, against a background of  $\sim 420,000$  events. The Li-Ma statistical significance (Li & Ma 1983) of this excess is  $+5.27\sigma$ . Of the 101 ON-OFF pairs, 65 pairs show an excess in their raw rates, while just 36 show a deficit.

Next, the trigger multiplicity was re-imposed. The total number of excess events after trigger re-imposition was 4551, with a background of  $\sim 350,000$ , for a total significance of  $+5.44\sigma$ . Seventy of the 101 pairs showed an excess of events from the source.

Finally, a cut on  $\chi^2/\text{ndf} < 1$  was applied on top of the trigger re-imposition cut. The remaining number of excess events was 4062. The background was reduced by a factor of approximately two, to  $\sim 180,000$  events, and the total significance of the signal increased markedly to  $+6.75\sigma$ . Of the 101 pairs, 77 now show an excess of events from the source region, while just 24 show a deficit.

The observed excess is statistically strong, being present at greater than the five standard deviation level in the raw trigger rates alone. Because STACEE is a new detector using a novel technique, there is the question of whether this excess is actually due to a gamma-ray signal, or whether it could be due to some unforeseen systematic effect that is present in spite of our efforts to closely match ON and OFF halves of each pair. This question will ultimately be decided by confirmation of the result by other experiments. Detection of other sources with this technique should provide further confirmation of the method. Nonetheless, there are consistency checks which can be performed to strengthen the conclusion that STACEE-32 sees gamma rays from the Crab.

The first and most powerful check is that the significance of the excess increases as selection cuts are applied to the data. Both the trigger re-imposition cut, and especially the cut on the  $\chi^2/\text{ndf}$ , increase the significance of the signal by amounts in agreement with expectations from simulation. In short, the observed excess behaves just as a gamma-ray signal should.

Secondly, one can look at the distribution of pairwise significances. The pairwise significance

is defined as the observed excess or deficit, in standard deviations, for each ON-OFF pair. For a steady source with a constant flux, the distribution of pairwise significances should be normally distributed, with unit width and a shifted mean. As is seen in Figure 5, the distribution of pairwise significances for our data does have the expected form. This fact further supports the interpretation of the excess as a gamma-ray signal.

In Table 3, the data have been broken down by month. Since fewer runs were taken in January and February of 1999, these months have been combined. An excess with a significance of  $\sim 4\sigma$  is seen in each era. Also noteworthy is that the background rate (OFF events per unit time) decreased by 20% between the November data and the December-February data. We interpret this decrease as an increase in the energy threshold of the experiment. Closer examination of the data shows that the rates were steady within the month of November, and within December as well. Whatever change happened to the detector must therefore have occurred during the intervening full Moon period during which STACEE did not operate. Although the reason for this increase in threshold is not known with certainty, we suspect that the angular pointing of the heliostats drifted slightly out of alignment, decreasing the optical throughput.

## 5.2. Pulsed Emission Search

Having established the presence of a gamma-ray signal in our data, we then carried out a search for pulsed emission in phase with the Crab Pulsar’s emission. A GPS clock recorded the arrival time of every event with an accuracy of  $\sim 1\mu\text{s}$ . The arrival time of each event at Earth was corrected to barycentric dynamical time (TDB) using the JPL Planetary and Lunar Ephemerides DEC-200 package (Standish 1997). The corresponding radio phases were obtained from the Jodrell Bank ephemeris (Lyne, Pritchard, & Roberts 1999). The phase values were interpolated between monthly epochs by expanding the phase in a Taylor series, and by requiring continuity of the phase, period, and time derivatives of the period at the midway point between the two months. The barycentering and ephemeris calculations were checked by applying them to optical pulsar data recorded by the Whipple gamma-ray collaboration. For these data, we verified that the optical pulse was extracted properly.

The arrival times of on-source events were then folded with the pulsar phase to produce a phase histogram for the STACEE-32 data. Figure 6 shows the phase histogram for on-source events passing all event cuts. No obviously significant structure is seen. We have applied the H-test to test the uniformity of the phase histogram (de Jager, Swanepoel, & Raubenheimer 1989; de Jager 1994). The test yields a value for the  $h$  parameter of 5.37, which has a chance probability of 0.12. We therefore conclude that STACEE-32’s Crab phase histogram is consistent with being uniform in phase.

Concluding that our data set contains no strong evidence of pulsed emission, we then set an upper limit on the pulsed fraction of the total observed excess. Because the pulse profile of

the pulsed emission at STACEE’s energies is unknown, we make an assumption about the phase intervals in which the gamma-ray emission would occur. We assume that the pulsed emission at STACEE energies would occur in phase with the pulsed emission seen by EGRET (Nolan et al. 1993; Ramanamurthy et al. 1995; Fierro et al. 1998). We defined an “on-pulse” region for the phase histogram, which includes an interval centered about the main radio pulse at 0.94-0.04 of the phase histogram, and a second interval about the intrapulse from 0.32-0.43. Using the method of Helene (1983), we derive an upper limit on the pulsed fraction of  $< 5.5\%$  of the observed excess, at the 90% confidence level. Table 4 contains the event totals for the on-pulse and off-pulse regions.

### 5.3. Energy and Integral Flux Result

The energy threshold and integral flux for these data must be determined from careful calibration and simulations of all parts of the detector. STACEE-32 used three simulation packages to model the response of the instrument to gamma rays. The well-established MOCCA code was used to model extensive air showers and Cherenkov light production (Hillas 1985). A complete ray-tracing program followed the paths of photons through the optics. Finally, a detailed electronics simulation which made use of a library of digitized PMT pulses was used to model the performance of the PMTs and electronics. All parts of the simulations have been verified against calibration data.

For the purpose of determining an energy threshold and integral flux, only data taken in November 1998 were used. As explained in § 5.1, these data had the lowest energy threshold, as measured by the trigger rates. Also, the detector was carefully aligned during this month. During the subsequent months, it is believed that small degradations in the alignment increased the energy threshold, but we do not have enough information to track the effect reliably. Using only data from November 1998 therefore provides the lowest possible energy threshold and minimizes possible systematics associated with optical alignment. The increased statistical uncertainty from using a subset of the data as opposed to the entire data set is still smaller than the systematic uncertainty on the flux. Likewise, we have used the total rates before event cuts in determining the energy threshold and integral flux, since the efficiencies of these cuts depend on the simulation, and so would introduce additional systematic uncertainties if included.

Monte Carlo simulations were used to determine the sensitivity of STACEE-32 to gamma rays. The sensitivity was calculated for gamma rays of various energies coming from multiple positions along the Crab’s trajectory across the sky. The results were expressed as an effective area curve, which is the gamma-ray collection area of STACEE-32 as a function of the gamma-ray energy. The average effective area curve for the November 1998 data was calculated by weighting each position on the sky by its exposure in the data set. Figure 7 shows the average effective area as a function of energy. The sensitivity of STACEE-32 starts at an energy below 100 GeV, and quickly rises with energy. The effective area approaches a plateau value of  $\sim 28,000 \text{ m}^2$  above 1 TeV.

To determine the energy threshold and integral flux, we assume that the Crab’s energy spectrum follows a differential power law of the form

$$\frac{dN}{dE} = CE^{-2.4}. \quad (3)$$

The power law index of  $-2.4$  is estimated from measured Crab spectra, interpolated to STACEE-32’s energy range (Hillas et al. 1998). Convolving this spectrum with the effective area curve yields the differential trigger rate per unit energy. The peak rate occurs at an energy of 190 GeV. This is our estimate for the so-called “spectral threshold energy.” The energy threshold changes by less than  $\pm 10$  GeV if the assumed spectral index is varied by  $\pm 0.2$ .

Estimates of the uncertainty in each element of the simulations (e.g. uncertainties in measured mirror reflectivities, PMT gains, etc.) yield a total systematic uncertainty on the energy of 32% ( $\pm 60$  GeV). No single factor dominates the systematic uncertainty.

For the November data, a total of 183,501 on-source events were seen in the raw data (without event cuts), versus 181,349 off-source events, in 56,056 s of observing time. The excess rate is therefore  $0.038 \pm 0.011$  Hz. By integrating the assumed differential flux with the effective area curve, and equating this to the observed rate, we determine the integral flux. We find that the integral flux of gamma rays from the Crab Nebula above our energy threshold of  $E_{th} = 190 \pm 60$  GeV is

$$I(E > E_{th}) = (2.2 \pm 0.6 \pm 0.2) \times 10^{-10} \text{ photons cm}^{-2} \text{ s}^{-1}. \quad (4)$$

Here the first error is statistical, and the second error is the systematic error on the flux itself, not including the effects of uncertainty in the energy threshold. The dominant systematic error is the uncertainty in the energy threshold  $E_{th}$ , which does not change the flux value itself, but which does change the energy at which that flux is reported.

## 6. DISCUSSION

Figure 8 shows STACEE-32’s integral flux value. Also shown for comparison are measurements from the CAT (Barrau et al. 1997) and Whipple (Hillas et al. 1998) experiments. Our measured flux is consistent with an extension to lower energies of the power law spectrum seen by Whipple. Inverse Compton models generally predict a hardening of the spectral slope as the energy decreases. Given the systematic uncertainties, our measurement is consistent with these expectations.

No evidence of pulsed emission from the Crab Pulsar is seen, and an upper limit on the pulsed fraction is derived at  $< 5.5\%$  (90% CL) of the observed signal. At present, the energy threshold of this limit, although lower than any previous limit, is not low enough to differentiate between Polar Cap and Outer Gap models. As the energy threshold of STACEE is lowered further, however, future limits should constrain the theoretical models.

This detection is the first for the STACEE instrument. The CELESTE collaboration, which

is operating its own solar heliostat experiment at the Thémis site in France, has reported a preliminary detection of gamma rays from the Crab using a similar technique. Their data analysis is in progress (Smith et al. 1998). Although STACEE-32 was a prototype instrument, it achieved an unprecedentedly low energy threshold. The full STACEE detector will be completed in the year 2000, and will feature twice as many heliostats, improved trigger electronics, and 1 GHz sampling waveform digitizers. Based upon the STACEE-32 results, we expect that the full STACEE instrument will obtain its design goal of an energy threshold of  $\sim 50$  GeV.

In the future, solar heliostat experiments such as STACEE, CELESTE (Giebels et al. 1998), and Solar Two (Zweerink et al. 1999) will provide complete spectral coverage at energies between  $\sim 50$  and 500 GeV for the Northern Hemisphere. These sorts of low threshold experiments will provide continuity between satellite measurements and ground-based detectors at TeV energies, and will naturally complement future satellite experiments such as GLAST.

We are grateful to the staff at the NSTTF for their excellent support. We thank the Physics Division of Los Alamos National Laboratory for loans of electronic equipment. We also thank the SNO collaboration for providing us with acrylic for light concentrators, and the machine shop staffs at Chicago and McGill for their assistance. The Whipple collaboration kindly provided us with optical pulsar data for testing our barycentering analysis. Many thanks to Tom Brennan, Katie Burns, Jaci Conrad, Jim Hinton, William Loh, Anthony Miceli, Gora Mohanty, Alex Montgomery, Heather Ueunten, and François Vincent. This work was supported in part by the National Science Foundation, the Natural Sciences and Engineering Research Council, FCAR (Fonds pour la Formation de Chercheurs et l'Aide à la Recherche), the Research Corporation, and the California Space Institute. CEC is a Cottrell Scholar of Research Corporation.

## REFERENCES

- Atoyan, A. M., & Aharonian, F. A. 1996, *MNRAS*, 278, 525
- Barrau, A., et al. 1997, in *Towards A Major Atmospheric Cherenkov Detector V* (Kruger Park), ed. O. C. de Jager (Potchefstroom, South Africa: Potchefstroom University), 166
- Chantell, M. C., et al. 1998, *Nucl. Instrum. Methods*, A408, 468
- Cheng, K. S., Ho, C., & Ruderman, M. 1986, *ApJ*, 300, 500
- Daugherty, J. K., & Harding, A. K. 1982, *ApJ*, 252, 337
- de Jager, O. C. 1994, *ApJ*, 436, 239
- de Jager, O. C., & Harding, A. K. 1992, *ApJ*, 396, 161

- de Jager, O. C., Harding, A. K., Michelson, P. F., Nel, H. I., Nolan, P. L., Sreekumar, P., & Thompson, D. J. 1996, *ApJ*, 457, 253
- de Jager, O. C., Swanepoel, J. W. H., & Raubenheimer, B. C. 1989, *A&A*, 221, 180
- Fierro, J. M., Michelson, P. F., Nolan, P. L., & Thompson, D. J. 1998, *ApJ*, 494, 734
- Giebels, B., et al. 1998, *Nucl. Instrum. Methods*, A412, 329
- Helene, O. 1983, *Nucl. Instrum. Methods*, 212, 319
- Hillas, A. M. 1985, in *Proc. 19th Int. Cosmic Ray Conf. (La Jolla)*, 1, 155
- Hillas, A. M., et al. 1998, *ApJ*, 503, 744
- Lessard, R. W., et al. 1999, *ApJ*, 531, L942
- Li, T. P., & Ma, Y. Q. 1983, *ApJ*, 272, 317
- Lyne, A. G., Pritchard, R. S., & Roberts, M. 1999, *Jodrell Bank Crab Pulsar Timing Results Monthly Ephemeris*, available from <http://www.jb.man.ac.uk/~pulsar/crab.html>
- Ning, X., Winston, R., & O’Gallagher, J., *Applied Optics*, 26, 300
- Nolan, P. L., et al. 1993, *ApJ*, 409, 697
- Ong, R. A., et al. 1996, *Astropart. Phys.*, 5, 353
- Oser, S. M. 2000, University of Chicago, Department of Physics, Ph.D. thesis (unpublished)
- Ramanamurthy, P. V., et al. 1995, *ApJ*, 450, 791
- Romani, R. W. 1996, *ApJ*, 470, 469
- Smith, D. A., et al. 1998, in *Proc. of the 19th Texas Symposium on Ultrarelativistic Astrophysics (Paris)*, ed. J. Paul, T. Montmerle, & E. Aubourg (Paris: CEA Saclay)
- Standish, E. M. 1997, *JPL Planetary and Lunar Ephemerides*, available from <ftp://navigator.jpl.nasa.gov/pub/ephem/>
- Weekes, T. C. 1988, *Phys. Rep.*, 160, 1
- Zweerink, J. A., et al. 1999, in *Proc. 26th Int. Cosmic Ray Conf. (Salt Lake City)*, 5, 223

Fig. 1.— STACEE Detector Concept Drawing. An array of heliostat mirrors collects Cherenkov light produced in a gamma-ray air shower. The heliostats reflect the light to secondary mirrors located on a central tower. The secondary mirrors image the light from each heliostat onto an individual photomultiplier tube. The STACEE-32 prototype used 32 heliostats and two secondary reflectors. This diagram is not to scale.

Fig. 2.— Arrangement of Heliostats at the National Solar Thermal Test Facility. Two secondary mirrors (not shown) on the central tower view sixteen heliostats each. One secondary mirror views the east half of the field, and one views the west. The four subclusters of eight heliostats each correspond to the four trigger groups described in § 2.

Fig. 3.— Cherenkov Photon Yields versus Energy for Different Species. Plotted is the mean Cherenkov photon density within 125 m of the shower core for vertically incident showers. Only photons with wavelengths between 300-550 nm which land within a 10 ns window around the peak arrival time are included.

Fig. 4.— Timing Wavefront Shapes for Simulated Gamma-Ray and Proton Showers. Plotted is the arrival time of the Cherenkov photons on the ground, in nanoseconds, versus the location on the ground, in meters. Gamma-ray showers are approximately spherical near the center of the shower (becoming more conical towards the edges), while cosmic rays produce irregular, less spherical Cherenkov wavefronts.

Fig. 5.— Distribution of Pairwise Significances for the STACEE-32 Crab Data. The pairwise significance is defined as the observed excess or deficit, in standard deviations, for each ON-OFF pair. For a steady gamma-ray signal, the distribution of pairwise significances should be a Gaussian distribution with unit width. The significances are for event totals after all event cuts.

Fig. 6.— STACEE-32 Crab Pulsar Phase Histogram. The arrival times of on-source events are binned according to the radio phase of the Crab Pulsar. This plot includes all events passing the trigger re-imposition and shower sphericity event cuts. The main radio pulse occurs at a phase of zero. The horizontal dashed line is a fit to a uniform phase distribution.

Fig. 7.— Average Effective Area Curve for November 1998 Crab data set. The error bars are statistical only.

Fig. 8.— STACEE-32 Integral Flux Result for Crab Nebula. Also shown for comparison are the integral flux from the CAT experiment and the measured spectrum from the Whipple Observatory. The error bars on the STACEE-32 point include systematic error on the energy threshold, and systematic and statistical errors on the flux. The CAT data point includes only statistical error on the flux.



Table 1: Summary of Run Cuts.

Total pairs	141
<b>Runs Cut:</b>	
Clouds	6
Sky Clarity	1
Pressure Front	1
Frost	4
DAQ Malfunctions	2
Major Heliostat Malfunctions	5
High/Fluctuating Subcluster Rates	20
Abnormally Low Rate	1
Remaining Pairs	101

Table 2: ON–OFF Excesses for Crab Data Set.

	Raw	Trigger	$\chi^2/\text{ndf}$
Quantity	Data	Re-imposed	Cut
ON Events	426975	352030	182915
OFF Events	422115	347479	178853
Excess (ON–OFF)	4860	4551	4062
Significance	+5.27 $\sigma$	+5.44 $\sigma$	+6.75 $\sigma$
Pairs +/–	65/36	70/31	77/24

---

Note. — ON-OFF event tallies are shown for the raw data (no event cuts, but corrected for deadtime), after a trigger re-imposition cut, and after an additional cut on the sphericity of the shower wavefront. “Pairs +/–” refers to how many pairs showed an excess of events (+), versus a deficit (–).

Table 3: Monthly Crab Excesses.

Quantity	Nov	Dec	Jan/Feb	Total
On-source Time (s)	56056	51239	48040	155335
ON Events	76235	55634	51046	182915
OFF Events	74686	54342	49825	178853
Significance	$3.99\sigma$	$3.90\sigma$	$3.84\sigma$	$6.75\sigma$
Excess Rate ( $\text{min}^{-1}$ )	$1.66 \pm 0.42$	$1.51 \pm 0.39$	$1.52 \pm 0.40$	$1.57 \pm 0.23$

---

Note. — Results are shown with all event cuts applied (trigger re-imposition and cut on wavefront sphericity). The January 1999 and February 1999 data have been combined, since fewer runs were taken in these months.

Table 4: Pulsed Emission Search Results.

Number Of Events In Pulse Region	38173
Number Of Events Outside Pulse Region	144742
Significance for Pulsed Region	$-1.37\sigma$
Pulsed Fraction Of Emission (90% C.L. Upper Limit)	$< 5.5\%$

---

Note. — The phase search interval is: (0.94-0.04, 0.32-0.43). The trigger re-imposition cut and a cut on the  $\chi^2/\text{ndf}$  for a spherical fit have been applied.



# STACEE Concept

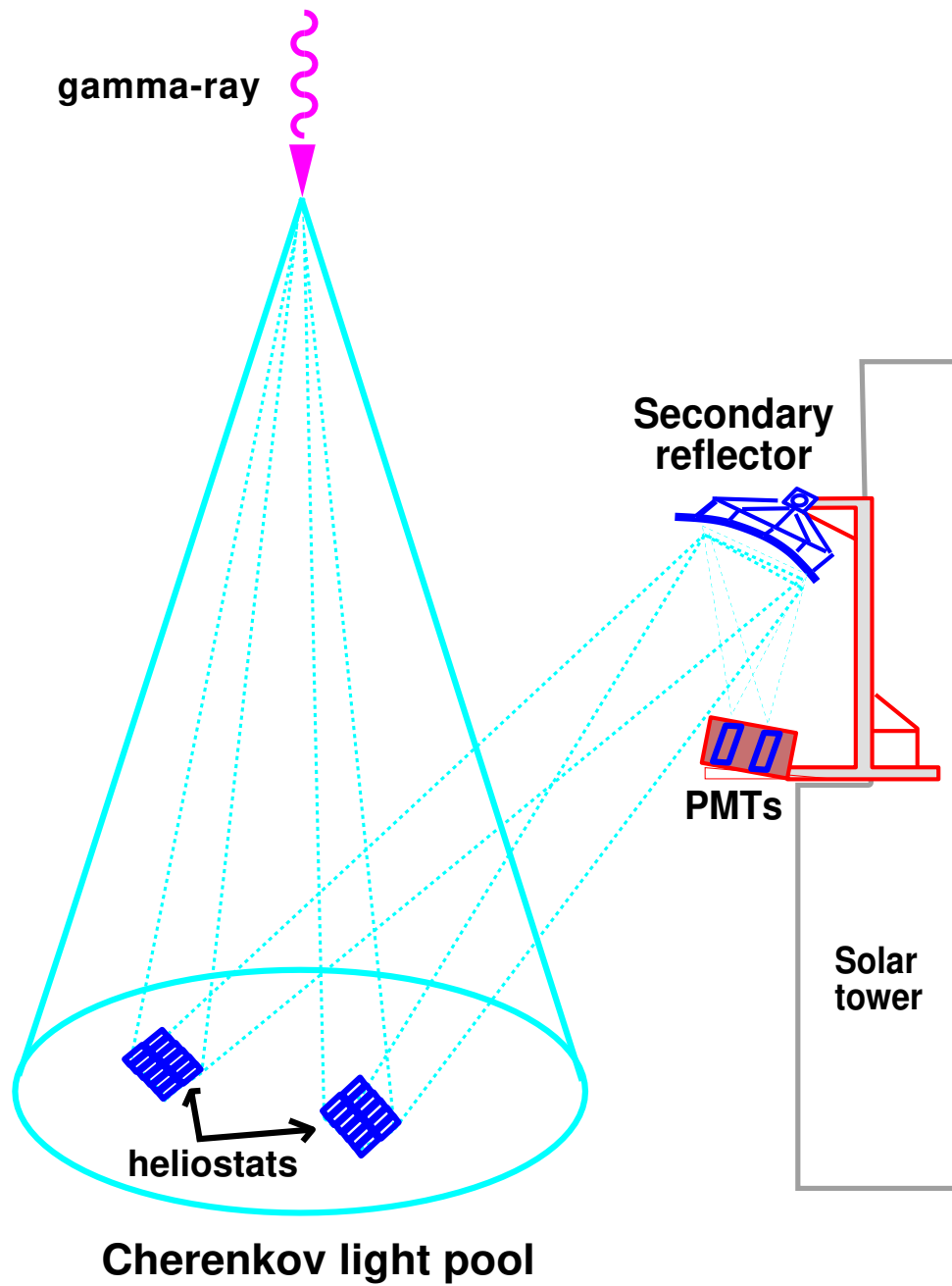


Fig. 1.—

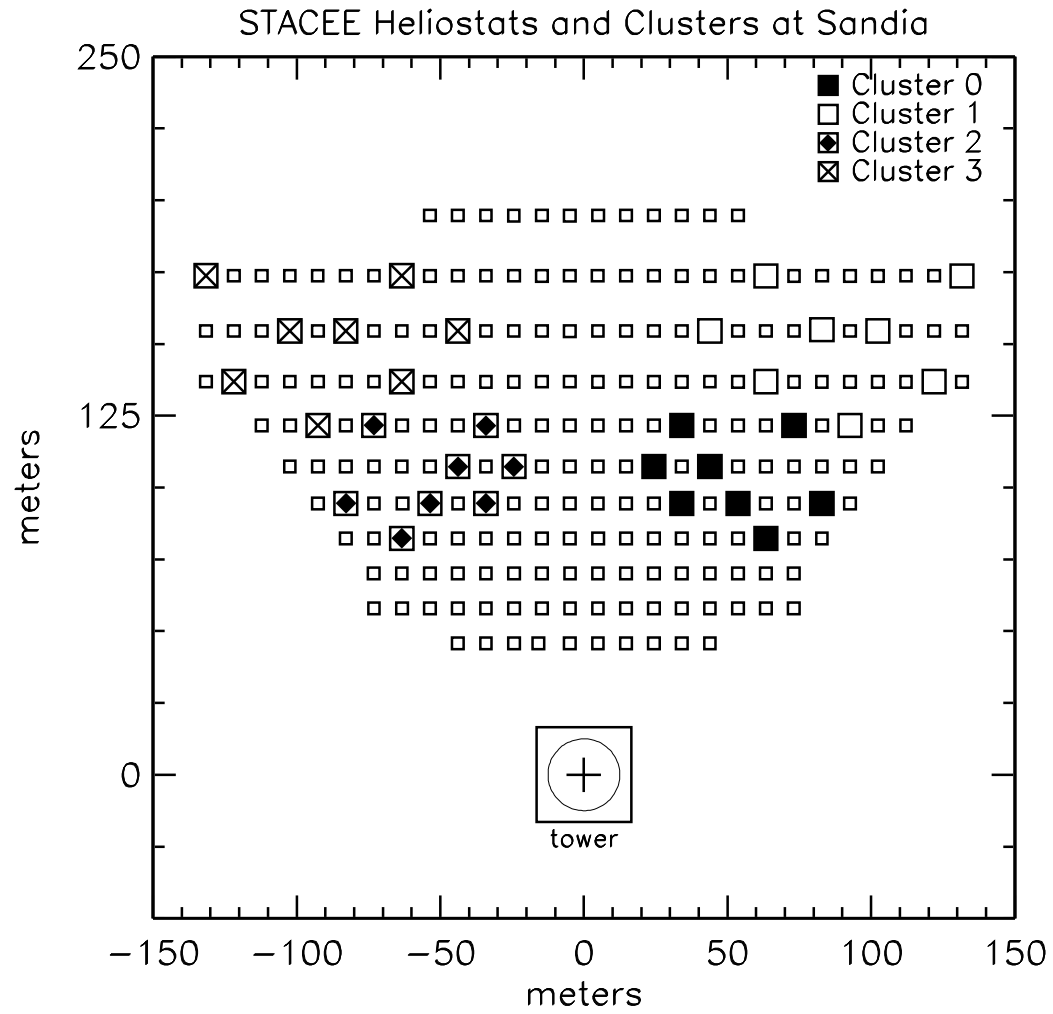


Fig. 2.—

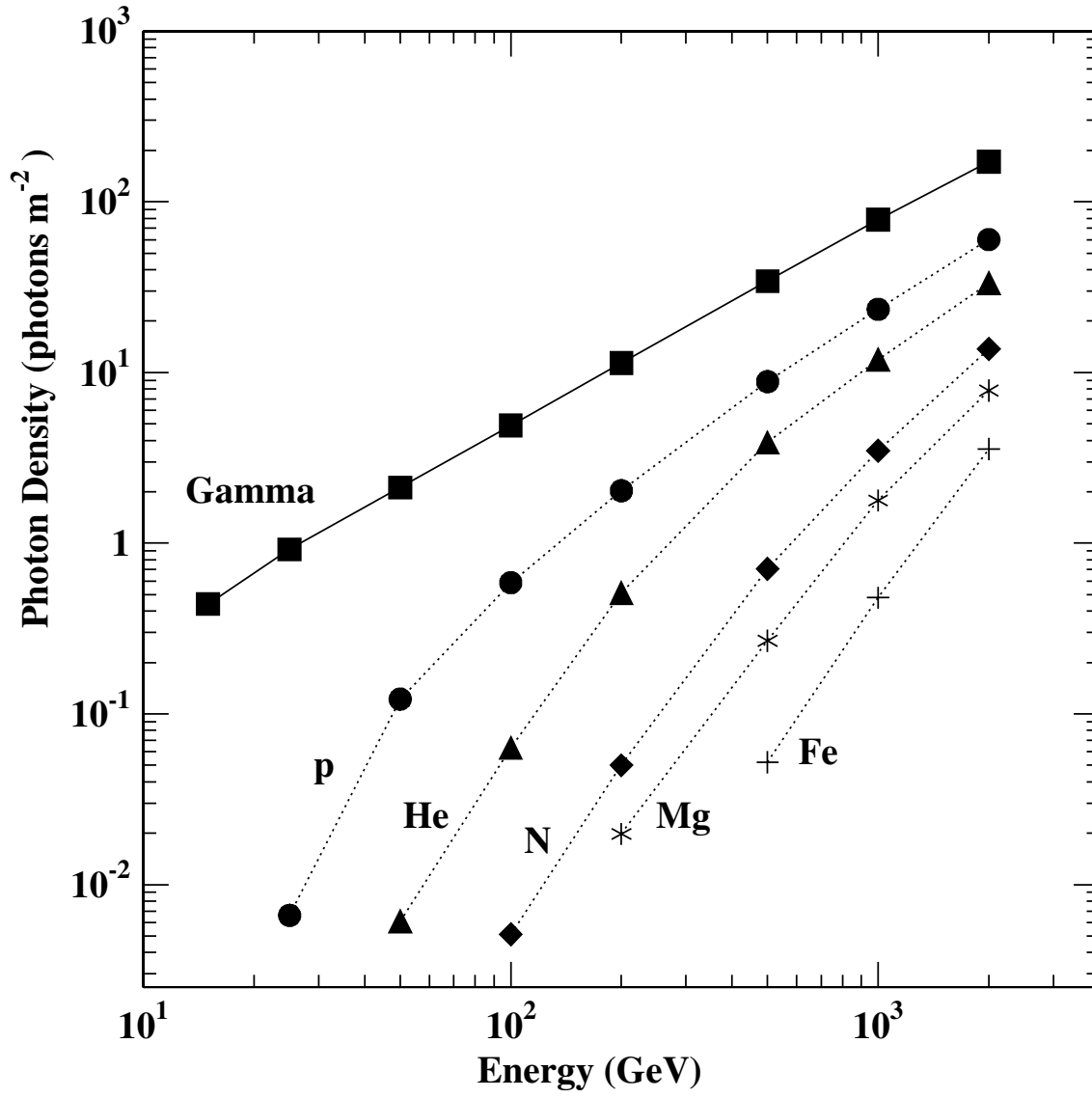


Fig. 3.—

### Simulated Shower Front Timing Profiles

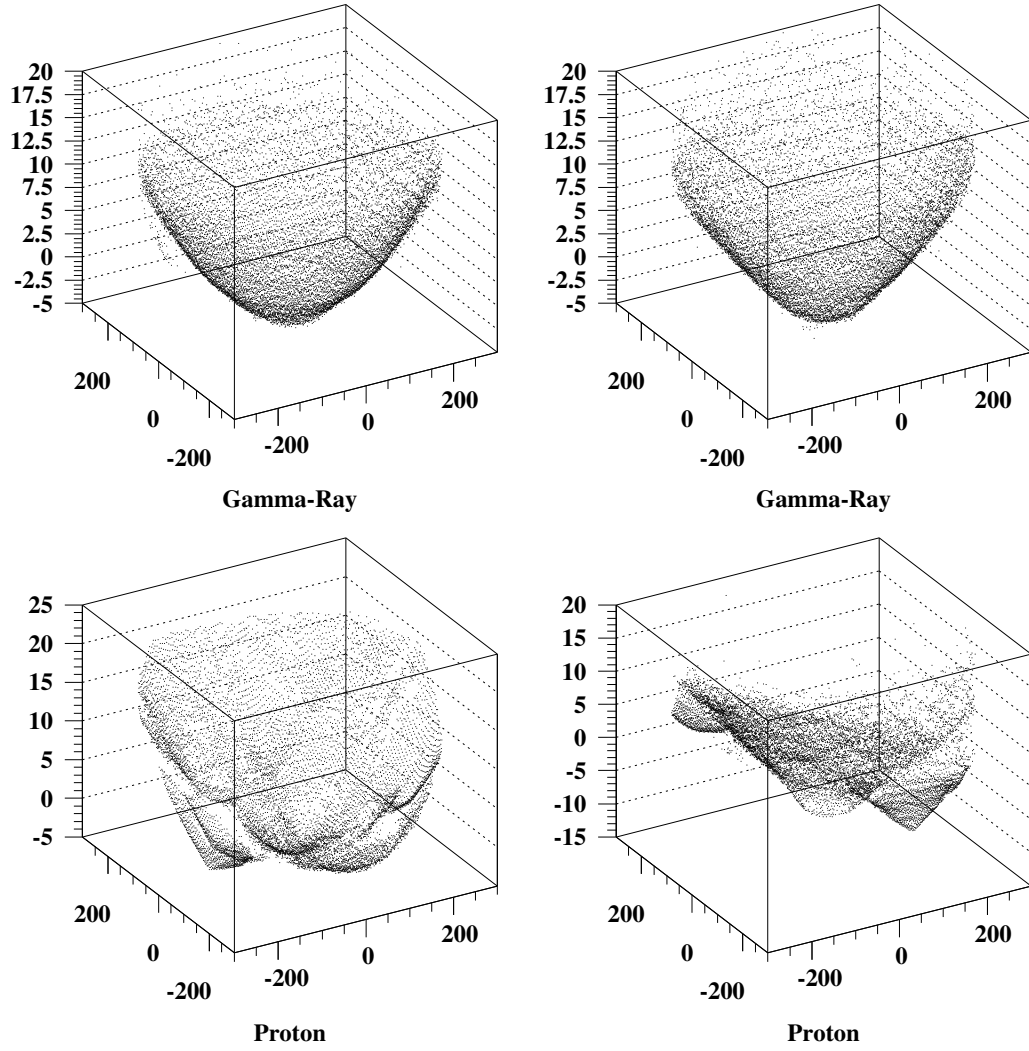


Fig. 4.—

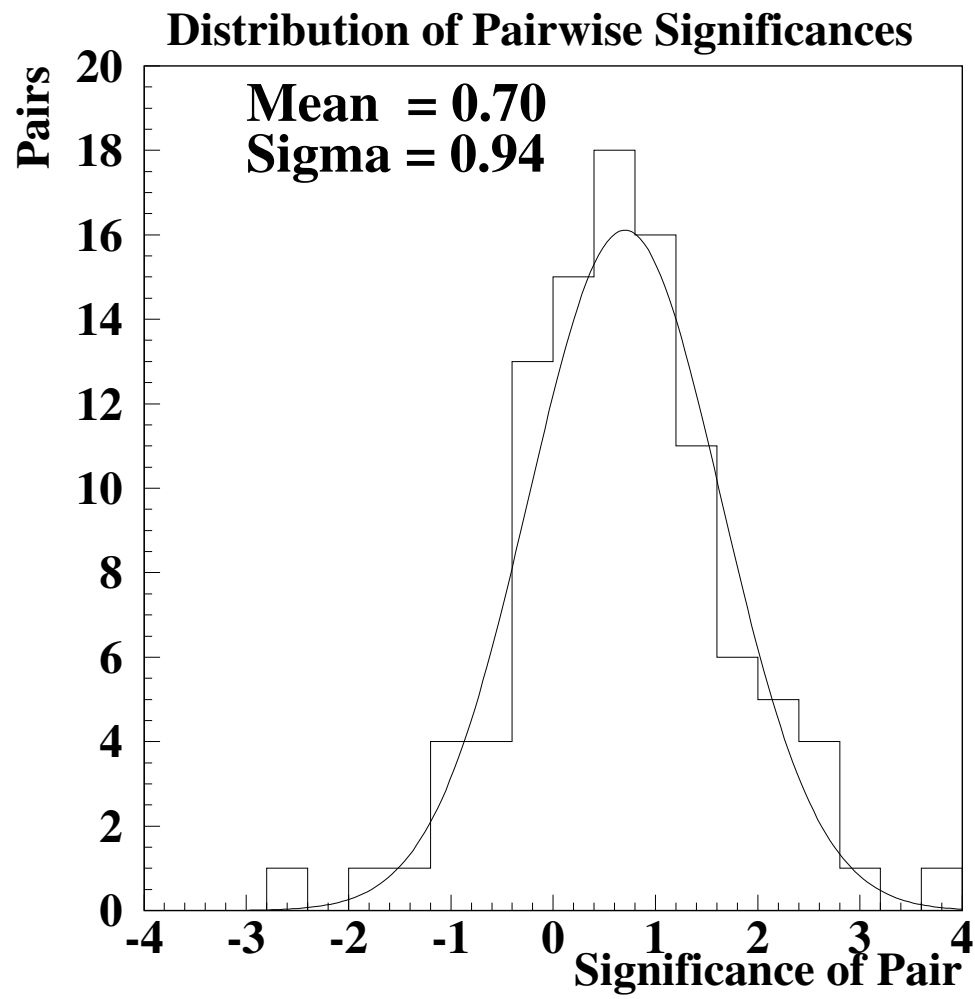


Fig. 5.—



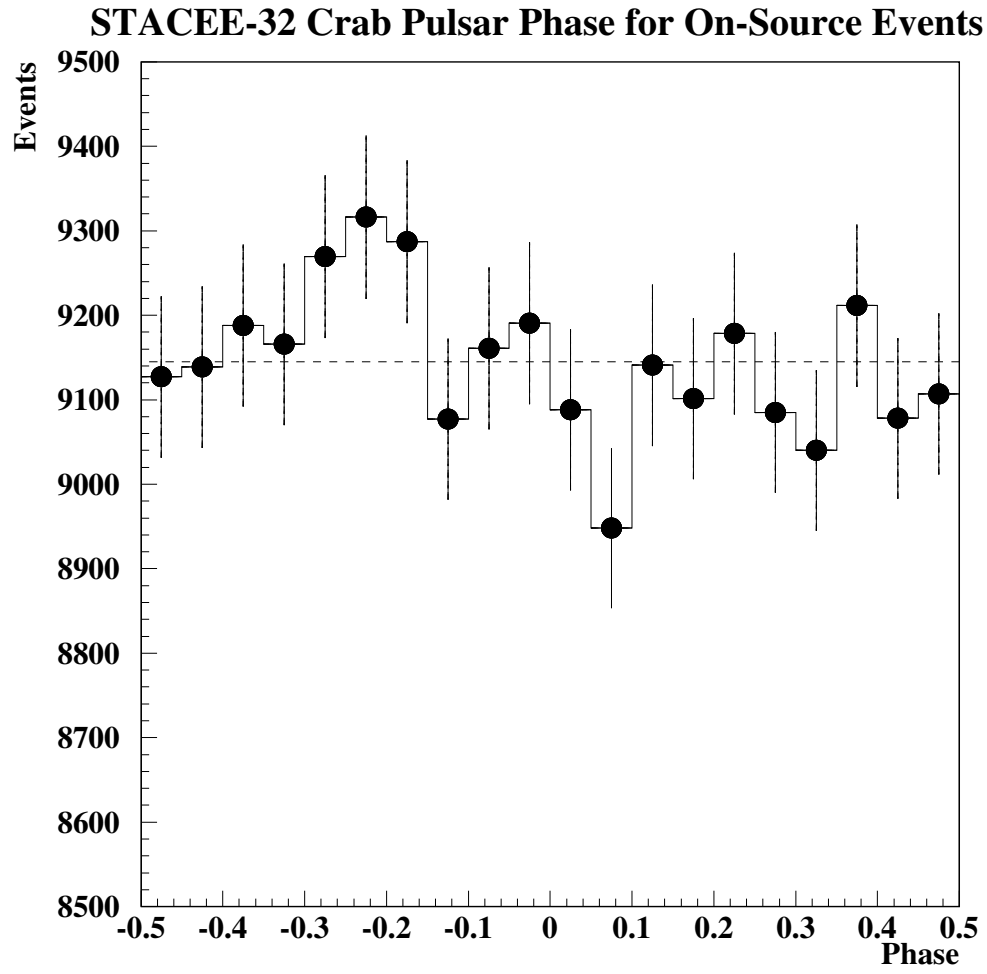


Fig. 6.—

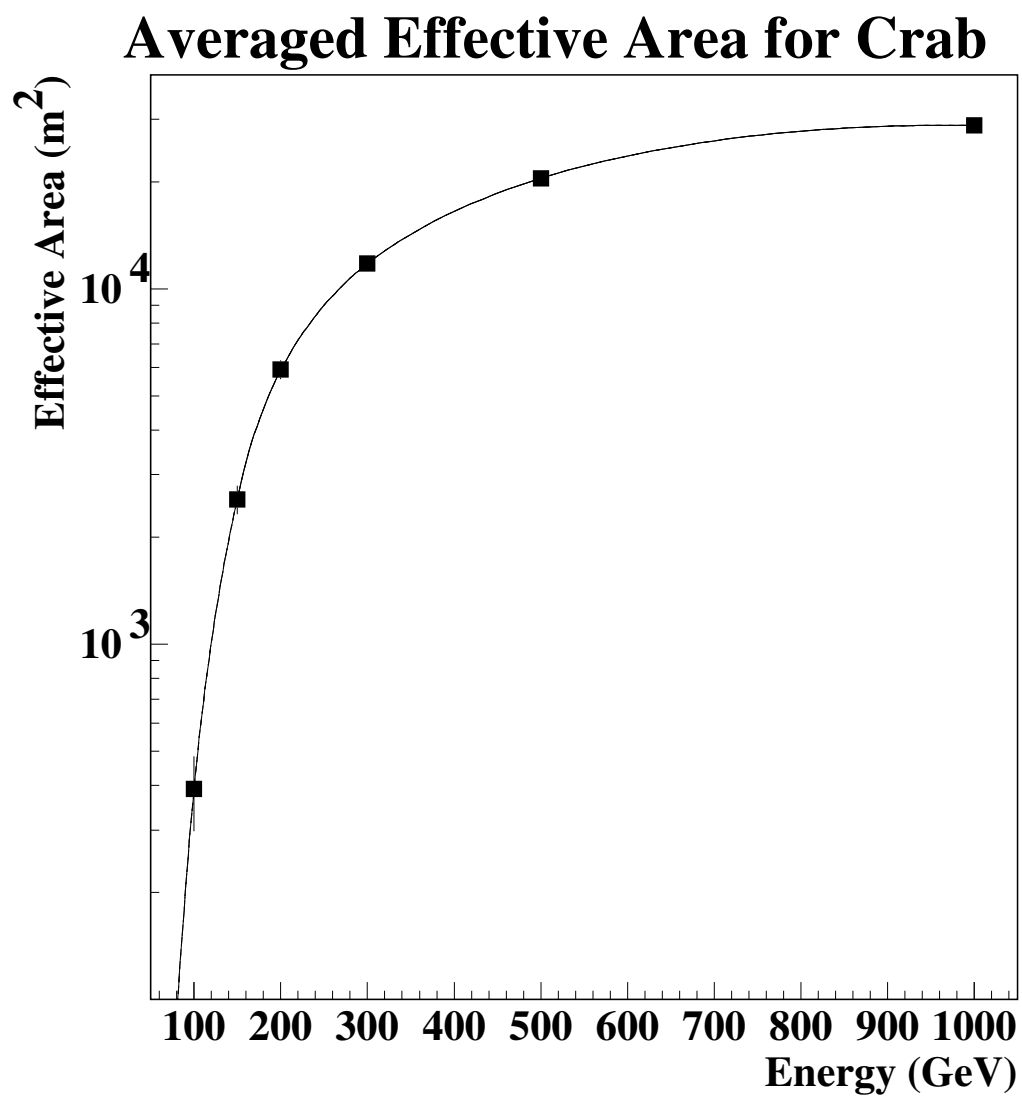


Fig. 7.—

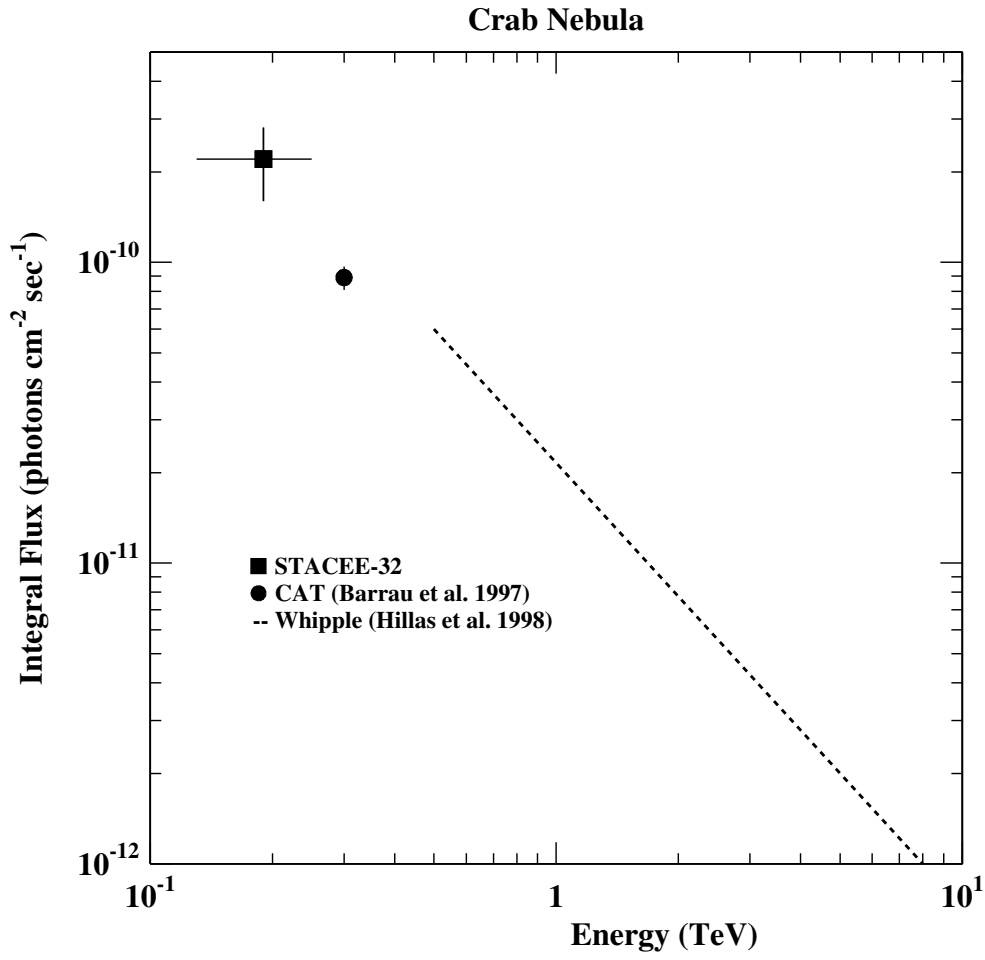


Fig. 8.—